Structures suggest an approach for converting weak self-peptide tumor antigens into superagonists for CD8 T cells in cancer

Pengcheng Wei[a,b], Kimberly R. Jordan[b,c], Jonathan D. Buhrman[b,c], Jun Lei[a], Hexiang Deng[d], Philippa Marrack[b,c,e], Shaodong Dai[b,c,f], John W. Kappler[b,c,f,1], Jill E. Slansky[b,c,1], and Lei Yin[a,b,1]

[a]Key Laboratory of Virology, Hubei Key Laboratory of Cell Homeostasis, College of Life Sciences, Wuhan University, 430072 Wuhan, China; [b]Department of Immunology and Genomic Medicine, National Jewish Health, Denver, CO 80206; [c]Department of Immunology and Microbiology, University of Colorado Anschutz Medical Campus, Aurora, CO 80045; [d]Key Laboratory of Biomedical Polymers, Ministry of Education, Institute for Advanced Studies, College of Chemistry and Molecular Sciences, Wuhan University, 430072 Wuhan, China; [e]Department of Biochemistry and Molecular Genetics, University of Colorado Anschutz Medical Campus, Aurora, CO 80045; and [f]Structural Biology and Biochemistry Program, University of Colorado Anschutz Medical Campus, Aurora, CO 80045

Tumors frequently express unmutated self-tumor–associated antigens (self-TAAs). However, trial results using self-TAAs as vaccine targets against cancer are mixed, often attributed to deletion of T cells with high-affinity receptors (TCRs) for self-TAAs during T cell development. Mutating these weak self-TAAs to produce higher affinity, effective vaccines is challenging, since the mutations may not benefit all members of the broad self-TAA–specific T cell repertoire. We previously identified a common weak murine self-TAA that we converted to a highly effective antitumor vaccine by a single amino acid substitution. In this case the modified and natural self-TAAs still raised very similar sets of CD8 T cells. Our structural studies herein show that the modification of the self-TAA resulted in a subtle change in the major histocompatibility complex I–TAA structure. This amino acid substitution allowed a dramatic conformational change in the peptide during subsequent TCR engagement, creating a large increase in TCR affinity and accounting for the efficacy of the modified self-TAA as a vaccine. These results show that carefully selected, well-characterized modifications to a poorly immunogenic self-TAA can rescue the immune response of the large repertoire of weakly responding natural self-TAA–specific CD8 T cells, driving them to proliferate and differentiate into functional effectors. Subsequently, the unmodified self-TAA on the tumor cells, while unable to drive this response, is nevertheless a sufficient target for the CD8 cytotoxic effectors. Our results suggest a pathway for more efficiently identifying variants of common self-TAAs, which could be useful in vaccine development, complementing other current nonantigen-specific immunotherapies.

T cell receptor | tumor-associated antigens | agonistic peptide | crystal structure | peptide–MHC–TCR interaction

Immunotherapy for cancer has yielded positive results for many patients (reviewed in refs. 1–3). Success with using checkpoint blockade inhibitors of CTLA-4 and PD1 proteins that naturally limit the activity and expansion of T cells specific for tumor-associated antigens (TAAs) is particularly striking (2). Checkpoint blockade therapy requires the presence of TAAs that can be recognized by infiltrating T cells. Some TAAs are neoantigens (neo-TAAs), formed by point mutations (4, 5), RNA splicing events or DNA translocations (6, 7), tumor-specific posttranslational modification of peptides (8), and peptide splicing unique to the tumor (9). Therefore, as a category these neo-TAAs can be considered "foreign" antigens, since the immune system does not experience them prior to the development of the tumor. The immunogenicity of these neo-TAAs is being tested in cancer vaccines to elicit antigen-specific T cell responses and to expand T cells for adoptive cell therapy (10–12). However, not all tumors express and present known neo-TAAs (reviewed in ref. 13).

Furthermore, most neo-TAAs are unique to each patient, making antigen-specific immunization not yet practical for large patient populations. Other classes of TAAs recognized by T cells consist of unmodified peptides derived from self-proteins, self-TAAs, that have become dysregulated in tumors (14). Self-TAAs are often shared by tumors arising from a specific organ across many patients. Unfortunately, vaccination trials using native self-TAA peptides or those modified to bind major histocompatibility complex I (MHCI) better have had limited success (reviewed in ref. 15), in part because self-tolerance mechanisms, such as central and peripheral tolerance and T cell anergy, have removed or inactivated the high-affinity T cells specific for these antigens (16). While increasing the binding of a self-TAA to MHCI can sometimes improve its immunogenicity (17, 18) and vaccine efficacy (19), this approach cannot usually overcome the inherent low affinity of the tolerized T cell receptor (TCR) repertoire, especially for those epitopes that already bind well to the MHC.

With the goal of expanding immunotherapies to a broader range of cancers, strategies for improving the function of low-affinity CD8 T cells specific for self-TAAs are needed. We chose the mouse CT26 tumor model to determine how to enhance responses to self-TAAs, because BALB/c mice carry an endogenous retrovirus, MuLV, which is poorly expressed in young somatic tissue but becomes highly expressed with age and in tumor cell lines, such as this colon carcinoma (20, 21). The immunodominant

Significance

Tumor vaccines using modified self-antigens that structurally enhance T cell receptor–peptide–major histocompatibility complex interactions greatly improve a T cell protective response against the tumor's unmodified self-antigen. X-ray crystal structures of these interactions explain how the native and modified peptides can interact with the same T cell receptor, but with different affinities and abilities to drive T cell proliferation and differentiation.

CD8 T cell response to CT26 is specific for GP70$_{423–431}$, also called the AH1 peptide, derived from MuLV and restricted by the MHCI molecule, H-2L^d (L^d). Despite the poor expression of GP70 in normal tissues, including the thymus, its presence nevertheless eliminates high-affinity AH1-specific CD8 T cells, leaving a heterogeneous, low-affinity repertoire, ineffective at targeting L^d-AH1 present on tumor cells (21). Immunization with the AH1 peptide using a variety of strong adjuvants induces a weak response by AH1-specific T cells, but they fail to expand sufficiently or to differentiate into cytotoxic T cell (CTL) effectors capable of preventing the growth of the CT26 tumor (22–24). Examination of CT26 tumor-infiltrating lymphocytes (TILs) in unimmunized mice shows the presence of AH1-specific CD8 T cells, although they are not differentiated into CTLs (25). Therefore, most of the cognate antitumor CD8 T cell repertoire left after negative selection consists of ineffective low-affinity T cells.

Previously, we showed how subtle amino acid substitutions within this noneffective self-TAA create superagonists that can expand a population of highly functional CTLs (24, 26, 27). Our results show that most of these CTLs arise from the native self-TAA low-affinity repertoire, as shown by expression of similar TCRs that encode a conserved motif in their CDR3β loop. These T cells are cross-reactive with the native self-TAA and effectively prevent tumor growth after activation with the substituted superagonist peptide. By comparing the peptide–MHC structures before and after binding to the TCR, we identify the structural basis for the improved antitumor immunity and discuss how this information might be used for an informed design of superagonists for other common shared self-TAAs.

Results

A Large Repertoire of CD8 T Cells Responds to Both the AH1 Peptide and Its Superagonist-Modified Peptide, A5. To improve the expansion, differentiation, and effectiveness of CD8 T cell responses to the CT26 tumor, in previous studies (24, 26–28) we screened peptide libraries to identify amino acid substitutions in AH1 that, when bound to the L^d molecule, have a much higher affinity than the native L^d-AH1 complex for an antigen-specific TCR. A set of peptides were identified with these properties. One of the peptides, A5, contained only a single amino acid change from the AH1 peptide and was effective in tumor prevention vaccines (24, 26). The results of these previous vaccination studies (24, 26–28) are summarized in Fig. 1A. Immunization of BALB/c mice with AH1 produced a poor expansion of AH1-specific CD8 T cells, only a small proportion of which differentiated into effector CTLs as judged by their interferon (IFN)-γ production in response to the AH1 peptide. These T cells did not control growth of a subsequently transplanted CT26 tumor. However, after immunization with the A5-substituted peptide, over 25% of the total splenic CD8 T cells bound the L^d tetramers bearing the immunizing A5 peptide. More importantly, about two-thirds of these activated tetramer-positive T cells cross-reacted with the unmodified AH1-L^d tetramer and most of these cross-reactive T cells produced IFN-γ in response to the AH1 peptide. These studies showed that the natural AH1 peptide was inefficient in driving the initial response of AH1-specific CD8 T cells, but that once fully expanded and differentiated by the stronger mutant A5 peptide, the AH1 peptide was a sufficient target for CTL to kill the tumor.

This effective antitumor response led us to use high-throughput sequencing to compare the CD8 T cell repertoires among the CT26 tumor-specific CD8 TILs, as well as the tetramer-binding CD8 T cells raised by immunization with the native, AH1, versus modified, A5, peptides. Our data are summarized in Fig. 1 B and C using the sequencing data from the studies in Dataset S1. The AH1-L^d tetramer-binding T cells in the AH1- or A5-immunized mice revealed many TCRs using members of the Vβ8 (TRVB13) family, especially Vβ8.1 and Vβ8.3, and often using the Jβ2.6 (TRBJ7) joining segment with a similar motif at the tip of a
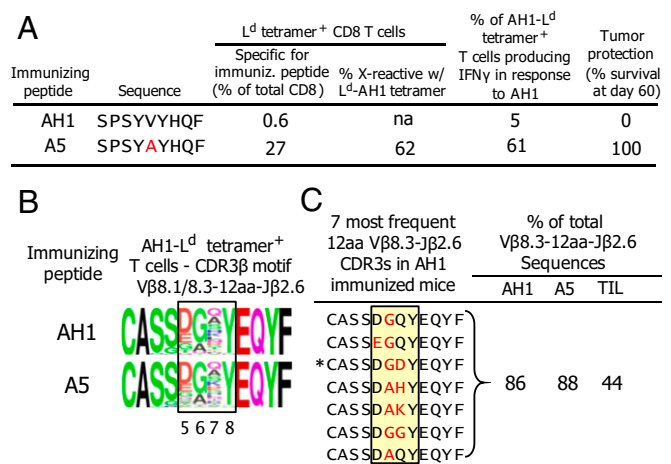
Fig. 1. The A5 peptide is a better immunogen than the native AH1 peptide and raises a repertoire similar to the native AH1 peptide. (A) Summary of previous data comparing the specificity and function of splenic CD8 T cells after BALB/c mice were vaccinated with the AH1 or A5 peptide. Columns 1 and 2 show the name and amino acid sequence of immunizing peptides. The red A highlights the valine to alanine amino acid substitution. Column 3 shows the percent of splenic CD8 T cells detected with fluorescent L^d tetramers loaded with the immunizing peptide ($n = 3$). Column 4 shows the percent of the T cells in column 3 that costain with the AH1-L^d tetramer. Column 5 shows the percent AH1-L^d tetramer binding cells that produced intracellular IFN-γ after restimulation of splenic CD8 T cells from the AH1- or A5-immunized mice with the AH1 peptide ($n = 3$). Column 6 shows the percent of immunized mice that survived for 60 d after a challenge with the CT26 tumor (AH1 $n = 10$, A5 $n = 10$). (B) A common motif was identified sequencing the CDR3β loop of the TCRs of the AH1-L^d tetramer binding CD8 T cells produced by immunization with the AH1 or A5 peptide. Sequences that occurred 10 or more times and contained a 12-amino acid-long CDR3 loops containing Vβ8.1 or Vβ8.3 with Jβ2.6 were used to create WebLogo amino acid frequency plots (70). The 4-amino acid motif (D/E, G/A, multiple amino acids, and Y) at the CDR3β tip is boxed. (C) The Vβ motif is particularly common in Vβ8.3$^+$ CD8 T cells in AH1- and A5-immunized mice and the TILs of tumor-bearing mice. The seven most frequent Vβ8.3 CDR3 sequences in B are shown. The common motif is boxed, and the amino acids encoded in part by nongermline bases are in red. These sequences account for a high percentage of the total motif containing Vβ8.3 sequences in AH1- ($n = 11,871$) or A5- ($n = 17,176$) immunized mice and nearly half of the motif bearing sequences found among CT26 TILs. The starred sequence is that of the 1D4 TCR CDR3β loop discussed below. A summarizes results from previous publications from this group (24, 26–28). The sequence analyses in B and C were performed with previously published data (27, 28) combined with additional new data. The list of combined sequences used is presented in Dataset S1.

12-amino acid CDR3β loop (Fig. 1B). Many of the TCR-β chain sequences containing this motif were shared among the most-frequent sequences obtained from peptide-immunized mice. For example, we obtained ~11,500 TCR Vβ sequences bearing Vβ8.3-Jβ2.6 with a 12-amino acid (12AA) CDR3β from AH1-L^d tetramer-binding T cells obtained from AH1-immunized mice. These encompassed ~200 unique sequences, but 7 accounted for 86% of the total sequences (Fig. 1C). These same seven Vβ sequences also accounted for 88% of the Vβ8.3–12AA–Jβ2.6 sequences from the A5-immunized mice and 44% of the AH1-specific sequences found in the TILs of unimmunized mice bearing the CT26 tumor. We picked the 1D4 T cell (asterisk in Fig. 1C) for our structural experiments below, because it bore this Vβ CDR3 motif and its Vβ CDR3 sequence was detected in both of the immunized mice and in TILs. In addition, this TCR used Vα6, a Vα found in the majority of T cell clones isolated from mice immunized with several of the variants of AH1 that were protective against the tumor in immunization trials (24, 26, 27). Thus, the effectiveness of immunization with the A5 peptide was not because it raised a new set of AH1-specific T cells, but rather

because they drove the expansion and differentiation of AH1 cross-reactive T cells similar to those raised by immunization with the AH1 peptide or those present in the tumors of unimmunized mice.

The AH1/A5 Cross-Reactive CD8 T Cells Have a Higher Affinity for A5-L^d. We postulated that, like other AH1-specific T cells we have analyzed previously (23, 24), the protective cross-reactive T cells described in Fig. 1 should have a higher affinity for the L^d-A5 ligand than for the natural unmodified L^d-AH1 ligand. We used two approaches to test this idea. First, we prepared a soluble version of the representative cross-reactive 1D4 TCR mentioned above, and whose TCR components are shown in (Fig. 2A). We used flow cytometry with a biotinylated, fluorescent, multimeric version of the TCR to assess its binding to insect cells (SF9) expressing on their surface L^d covalently linked to either AH1, A5, or a control peptide from β-galactosidase (βgal) (Fig. 2B). As expected, binding of the TCR tetramer to L^d-AH1–bearing cells was poor, but detectable, above the autofluorescence seen with L^d bound to the control peptide. However, the binding was much stronger to L^d with the A5 peptide.

For the second approach, we used surface plasmon resonance (SPR) to measure the kinetics of the interactions between the 1D4 TCR and its ligands. We prepared recombinant soluble versions of L^d complexed with β2m and either the AH1, A5, or the βgal control peptide. The complexes contained a C-terminal biotinylation tag, which was used to immobilize them in separate flow cells of a BIAcore streptavidin BIAsensor chip (Fig. 2C). Various concentrations of soluble 1D4 TCR were injected through the flow cells. The SPR signal (resonance units, RU) was corrected for the fluid-phase SPR signal using the flow cell containing the control L^d-βgal complex. While binding by the TCR to the native L^d-AH1 complex (Fig. 2 C, Left) was observed, the signal was too weak to calculate a binding affinity accurately. Based on the signal at equilibrium with maximum concentration of L^d-AH1, we estimated that the dissociation constant (K_D) was no better than 100 μM. In contrast, the TCR bound well to the L^d-A5 complex (Fig. 2 C, Center). The binding kinetics were second-order (Fig. 2 C, Right), fitting a model in which conformational changes in the complex occur after initial binding of the TCR, converting a rapidly dissociating complex into a more stable one, leading to an overall apparent K_D of ~8 μM. To confirm these second-order kinetics, we reversed the components (i.e., the TCR was immobilized in the flow cell and soluble L^d-A5 was injected) (Fig. 2D). Again, biphasic kinetics were observed with an apparent overall dissociation constant of ~14 μM. These results confirmed that the higher vaccination activity of L^d-A5 compared to L^d-AH1 was at least partly explained by its higher affinity for the relevant T cells, and they suggested that a conformation change in the complex upon TCR binding might account for the higher apparent affinity.
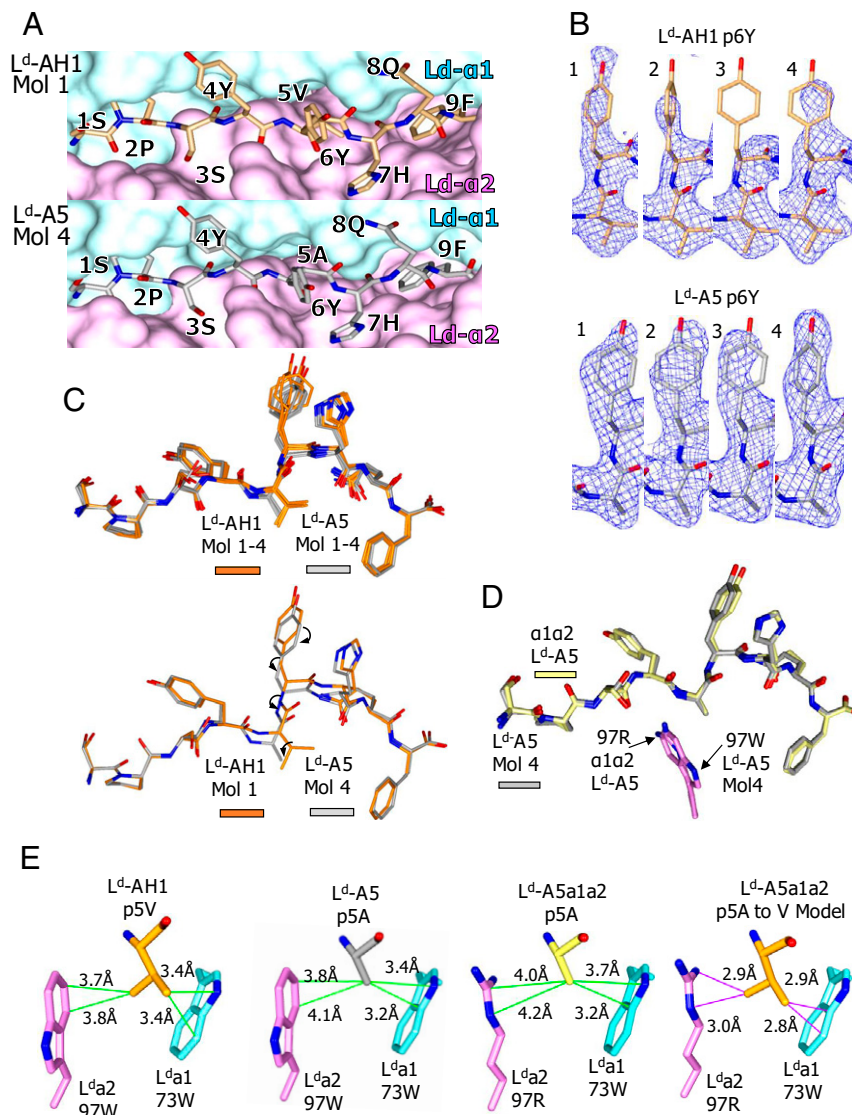
Structural Differences between the AH1 and A5 Peptide Bound to L^d. To determine the structural basis of this increase in activity, we prepared β2m and the extracellular domains of L^d in bacterial inclusion bodies. The proteins were solubilized, mixed, and refolded in the presence of excess AH1 or A5 peptide to obtain soluble L^d–β2m–peptide complexes. The proteins were crystallized, yielding nearly identical crystals (*SI Appendix*, Fig. S1); their structures were solved to the same resolution of 2.6 Å (*Materials and Methods* and *SI Appendix*, Table S1).

In the crystals, the AH1 and A5 peptides bound similarly to the L^d molecule (Fig. 3A). As expected, the major peptide anchor amino acids were p2P and p9F, matching the previously established canonical peptide-binding motif for L^d (29). The side chains of these two amino acids, as well as of p1S and to some extent p3S, were deep within the peptide-binding groove and not readily available for TCR contact. The side chain of p5V in AH1 and substituted p5A in A5, as expected, also pointed down into
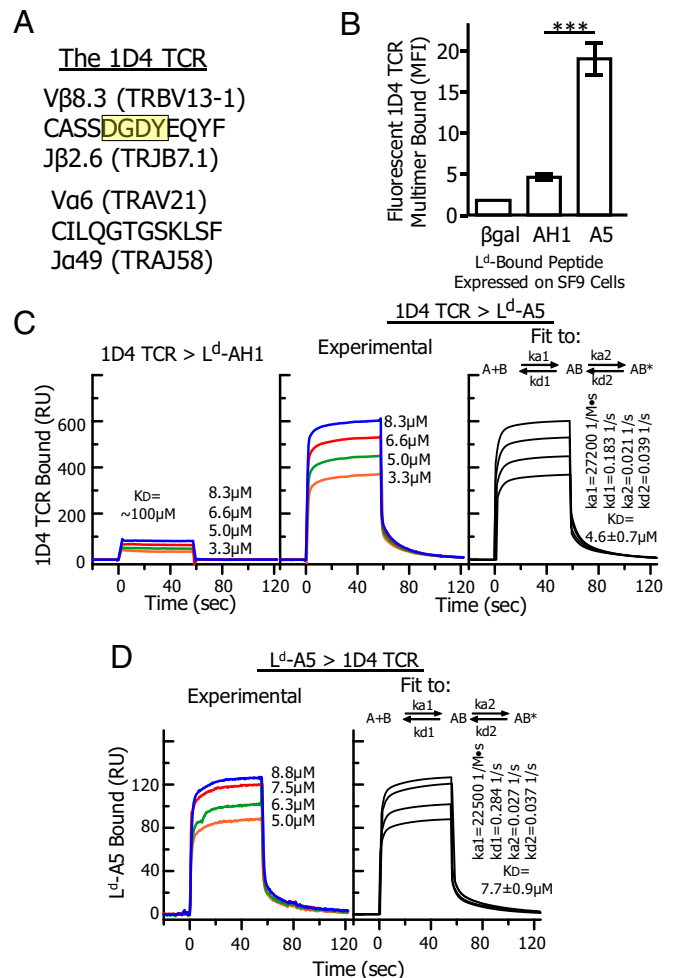
Fig. 2. Increased affinity of a typical AH1-specific TCR for the L^d-A5 complex compared to the L^d-AH1 complex. (A) Components of 1D4 TCR (starred in Fig. 1C) from an AH1-specific CD8 T cell, which bears the representative TCR Vβ motif (boxed), are shown. (B) Increased affinity of the 1D4 TCR for the L^d-A5 complex was demonstrated with fluorescent 1D4 TCR tetramers. A soluble fluorescent multimer version of the 1D4 TCR was prepared and used to detect L^d bearing a control βgal, AH1, or A5 peptide expressed on the surface of SF9 insect cells, gated for the same level of L^d. This experiment was performed three times in duplicate. The mean fluorescence intensity is shown for each with the SEM (***$P < 0.0001$). (C) Increased affinity of monomeric 1D4 TCR for L^d-A5 relative to L^d-AH1 was demonstrated with SPR. Biotinlyated L^d bound to AH1, A5, or control βgal peptide were immobilized in separate flow cells of a BIAcore biosensor chip. The indicated concentrations of soluble 1D4 TCR were injected for 1 min and binding to the ligands followed by the SPR signal (RU), which was corrected for the fluid phase signal used the flow cell with the L^d-βgal complex. (Left) The data from the L^d-AH1 flow cell. A dissociation constant was calculated to be >100μM from the equilibrium data. (Center) Data from the L^d-A5 flow cell showing strong binding by the L^d-A5 complex. (Right) The data in the Center panel were fit with the two-phase kinetics equation at the top of the panel, yielding an overall apparent K_D of ~8 μM. (D) To confirm, the biphasic binding kinetics of the components were reversed with the 1D4 TCR immobilized in the flow cells and the L^d-A5 complex injected. These data also showed strong binding of the L^d-A5 the TCR (Left) that fit with a similar two-phase binding reaction (Right) with a similar overall apparent K_D of ~14 μM. These data are representative of three experiments and three preparations of both the TCR and MHC proteins.

the peptide-binding groove. We have referred to p5V as a minor anchor, since its substitution with A in the A5 peptide had no discernible effect on peptide-binding affinity to the L^d molecule (24). The side chains of the remaining amino acids (p4Y, p6Y,

Wei et al.
Structures suggest an approach for converting weak self-peptide tumor antigens into superagonists for CD8 T cells in cancer

PNAS | 3 of 10
https://doi.org/10.1073/pnas.2100588118

Fig. 3. Structural differences between the AH1 and A5 peptide bound to L^d. (*A*) Top view of the L^d-AH1 (*Upper*, orange carbons) and L^d-A5 (*Lower*, gray carbons) peptides looking down on the L^d peptide binding groove. Shown are the molecular surfaces of $L^d\alpha1$ (cyan) and $L^d\alpha2$ (magenta) plus a wire-frame representation of the AH1 and A5 peptides. (*B*) Weaker electron density for the p6Y side chains in the four molecules of L^d-AH1 vs. L^d-A5 crystals. Wire-frame representations, colored as in *A*, are shown for the four p6Y amino acids in the AH1 (*Top*) and A5 (*Bottom*) peptide bound to L^d. The 2Fo-Fc electron density is shown (blue mesh) contoured at 1 σ. (*C*) Wire-frame representations of the peptides in the four L^d-AH1 and four L^d-A5 complexes of each crystal are shown overlaid and colored as in *A* (*Top*). Same as *Top*, except showing only the one molecule indicated from each crystal and using arrows to show the movements of the p5 and p6 amino acids in A5 due to the p5V > A substitution (*Bottom*). (*D*) Overlay showing the nearly identical structures of the A5 peptide using one of the full L^d-A5 structures and the truncated $Ld\alpha1\alpha2$-A5 structure (yellow carbons). (*E*) Shown are the similar positions of the L^d-97W in the full L^d-A5 structure and the L^d-97R in the truncated $L^d\alpha1\alpha2$-A5 structure.

p7H, and p8Q) were exposed on the surface of the complexes. The L^d-AH1 and L^d-A5 crystals both had a group of four nonsymmetrically related molecules in their unit cells arranged identically in the two crystals. Therefore, for each crystal, the structures of four complexes in the group were solved independently. The exposed surface of the peptides did not contact other members of the group, giving us four unobstructed views of how the p5V-to-A substitution changed the structure of the complexes prior to TCR engagement.

When bound to MHCI, the N and C termini of peptides occupy fixed conserved positions at the ends of the binding groove, but the middle of the peptide can often meander within the groove or even bulge out of the surface, depending on the peptide length and its interactions with the MHCI molecule (30–32). Therefore, we looked at how the p5V-to-A substitution changed the peptide

structure near p5. The largest change at the surface of the complex was in p6Y. In the L^d-AH1 structures the side chain of p6Y had weak, variable electron density in the four molecules of the asymmetric unit, while in the L^d-A5 structure, electron density was clearer for the p6Y side chain in all four molecules, which took similar positions in all four L^d-A5 molecules (Fig. 3*B*). This correlated with the higher B-factors for the AH1 p6Y side chains compared to those of A5 (*SI Appendix*, Fig. S2). Since the backbone of the peptides was well defined in all of the structures (*SI Appendix*, Fig. S2), these results indicated that the p6Y side chain in the L^d-AH1 complex was not fixed in one position but became more restricted by the p5A substitution. A possible explanation for this change came from overlaying the backbones of the peptides in the four molecules of both asymmetric units (Fig. 3*C*). Mirroring the electron density and B-factors, the positions of the side chains

Wei et al.
Structures suggest an approach for converting weak self-peptide tumor antigens into
superagonists for CD8 T cells in cancer

of the p6Y were ill-defined in AH1 structures, but more homogeneous among the A5 structures. The p5A substitution had allowed the backbone of the peptide from p5 to p7 to shift down about 1 Å within the peptide-binding groove, pulling the p6Y side chain with it (arrows in Fig. 3D). This shift was accompanied by the stabilization of the p6Y in a fixed position.

Conformational Changes in the A5 Peptide Allow for Optimal Orientations of Its Side Chains upon Binding 1D4 TCR. The structures of the L^d-peptides raised the question of whether the stabilization of the exposed p6Y side chain of the A5 vs. AH1 peptide was directly recognized by the 1D4 TCR, accounting for its increased affinity for this complex or, alternatively, since our SPR data indicated a conformational change upon TCR binding to L^d-A5 (Fig. 2 C and D), the movement of the peptide backbone may have indirectly facilitated additional conformational changes in the peptide that stabilized TCR binding. To examine these alternatives, we attempted to crystallize the 1D4 TCR bound to the L^d-A5 complex, which contained the three extracellular domains of L^d plus β2m. These attempts repeatedly failed, so we tried a different approach. Crystal structures of peptides bound to a truncated version of L^d, containing only the α1 and α2 domains but lacking α3 and β2m, have been reported (33, 34), so we prepared the A5 peptide bound to this truncated L^d ($L^dα1α2$-A5). We were concerned whether the mutations that had been previously made in the $L^dα1α2$ construct to improve expression would change the A5 peptide structure. This was especially true for the 97W-to-R mutation in $L^dα1$, since this amino acid lies directly under the peptide at p4 and is part of the p5 side chain binding pocket. Therefore, we first solved the crystal structure of the $L^dα1α2$-A5 complex with 97R at a resolution of 1.8 Å (*SI Appendix*, Table S1) and compared its structure to the full L^d-A5 complex containing the unmutated 97W. Fortunately, the A5 peptides in the two structures were virtually identical (Fig. 3E). The R in this complex lay in the same position as the W it replaced and had no apparent effect on the surface structure of the A5 peptide. The higher resolution of the $L^dα1α2$-A5 showed unequivocally the same repositioning of p6Y side chain and lowering of the peptide backbone. New crystal trials with the 1D4 TCR and the $L^dα1α2$-A5 complex were successful and we solved the structure of the ternary complex at a resolution of 2.4 Å (*SI Appendix*, Table S1).

The general aspects of the 1D4 TCR interaction with the Ld-A5 ligand are shown in Fig. 4 and the detailed atom-to-atom contacts are listed in Dataset S2. Many of the features were like those seen commonly in TCR–MHC interactions. The TCR docked in the familiar diagonal orientation centered on the exposed critical p4Y and p6Y (Fig. 4A). However, compared to most TCR–MHC complexes, the TCR was shifted toward the Ldα1 helix (Fig. 4 B and C), pushing the CDR2β loop away from its usual interactions with this helix, while greatly increasing peptide interactions with the CDR2α loop (Fig. 4C). Interactions with the A5 peptide, especially the surface-exposed p4Y and p6Y, dominated the TCR footprint (Fig. 4D). These tyrosines, as well as tyrosines in the 1D4 CDR loops, are a particularly striking example of the importance of tyrosines in TCR interactions with their ligands, pointed out previously by us and others (35–39). Tyrosines in the L^d-A5 complex and to 1D4 CDR loops were involved in 70% of the total contacts (Dataset S2).
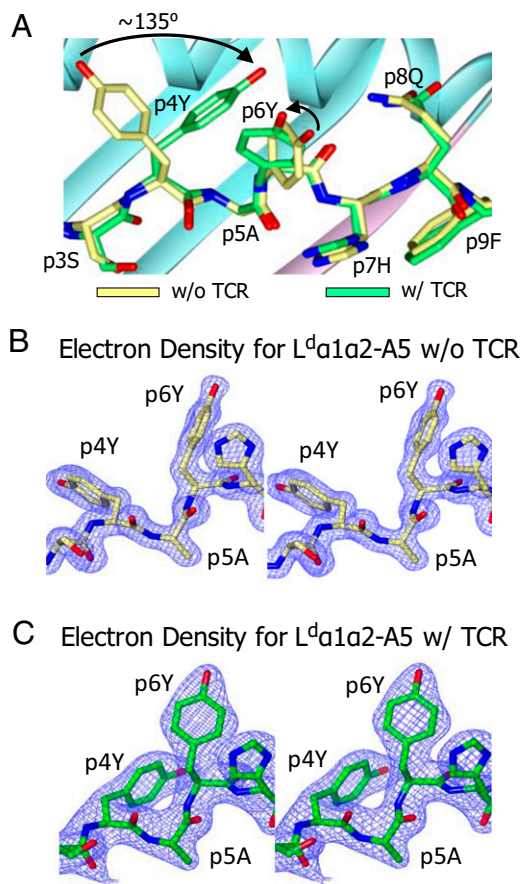
The structures showed a dramatic conformational change in p4Y and a smaller change in p6Y during the binding of the 1D4 TCR (Fig. 5). The structures of the A5 peptide in the $L^dα1α2$-A5 complex before and after engagement with the 1D4 TCR are overlaid in Fig. 5A. In the absence of the TCR, p4Y was pointed toward the N terminus of the peptide. Upon binding the TCR, its side chain made an ∼135° rotation toward the peptide C terminus. Meanwhile, the peptide backbone shift caused by the p5V-to-A substitution had prestabilized the p6Y side chain so that only a
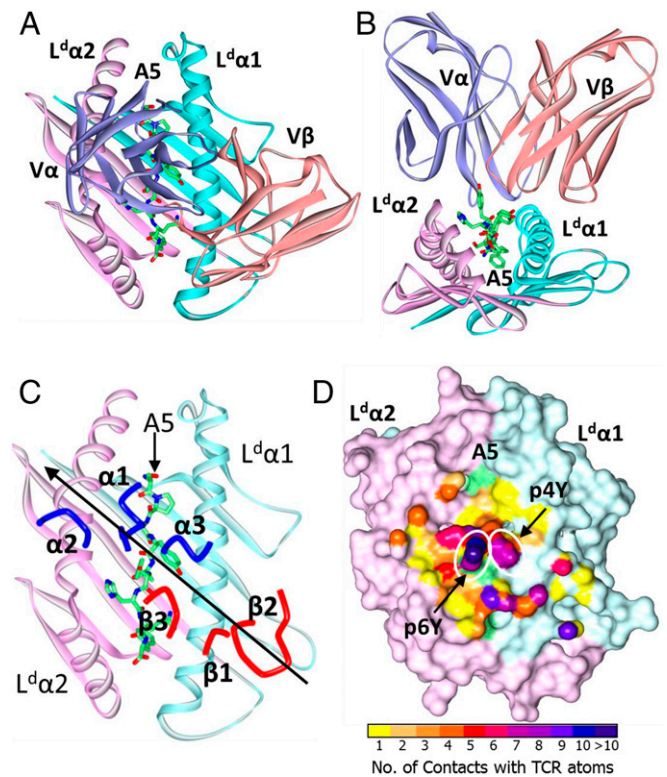
Fig. 4. Orientation of the 1D4 TCR on $L^dα1α2$-A5 and 1D4 TCR shifting over the $L^dα1$ helix. (A) Top view shows the diagonal orientation of the 1D4 TCR Vα and Vβ domains on the $L^dα1α2$-A5 complex: Ribbon representations of the 1D4 Vα (blue) and Vβ domains (red) as well as L^d-α1(cyan) and L^d-α2 (magenta) are shown. A wire-frame representation of the A5 peptide is also shown (green carbons). (B) The 1D4 TCR Vα and Vβ domains are shifted over the $L^dα1$ helix. The same representations as in A are shown except the view is from the C terminus of the A5 peptide looking down the peptide-binding groove. (C) Orientations of the six 1D4 TCR CDR loops on $L^dα1α2$-A5. The $L^dα1α2$-A5 complex is represented as in A and B. The tips of the six 1D4 TCR CDR loops are represented by tubes (blue tubes for Vα and red tubes for Vβ). The arrow between CDRα2, CDRβ3, and CDRβ1 on one side and CDRα1, CDRα3, and CDRβ2 on the other shows the diagonal orientation of the TCR on its ligand. (D) The footprint of the 1D4 TCR on the $L^dα1α2$-A5 ligand. The solvent-accessible surface of the $L^dα1$ (cyan), $L^dα2$ (magenta), and A5 peptide (light green) is shown. The footprint of the 1D4 TCR on the individual atoms forming the surface of the ligand are shown by changing the colors of the surface according to the number of contacts each ligand atom made to atoms in the TCR (atom-to-atom distances ≤4.5 Å). The positions of the peptide p4Y and p6Y amino acids on the surface are circled and labeled.

small rotational change was needed to accommodate the TCR. The clear electron density in the region of these tyrosines before (Fig. 5B) and after (Fig. 5C) TCR engagement documented these changes.

How these conformational changes are needed to engage the 1D4 TCR optimally are shown in Fig. 6. In Fig. 6A, the extensive repositioning of the p4Y side chain was required to avoid clashing with TCR Vα 29N and 92T (Fig. 6A, purple lines), while at the same time establishing contact with Vα 91G, 92T, and 93G, and Vβ 95D of the TCR via two H-bonds (Fig. 6A, green lines) at many van der Walls (vdW) bonds (Dataset S2). The new rotamer in p6Y upon TCR engagement perfectly aligned the p6Y side chain to be surrounded by a constellation of amino acids from CDR1α, CDR3α, and CDR3β (Fig. 6B), forming 50 vdW bonds as well as an H-bond to the Vβ CDR3 backbone. These conformational changes upon TCR binding could account for the biphasic binding kinetics of the TCR in Fig. 2 C and D. Overall, the repositioning of p4Y and p6Y allowed them to account for 30% of

Wei et al.
Structures suggest an approach for converting weak self-peptide tumor antigens into superagonists for CD8 T cells in cancer

PNAS | 5 of 10
https://doi.org/10.1073/pnas.2100588118

Fig. 5. Conformational changes in the A5 peptide during TCR engagement. (*A*) Conformational changes to p4Y and p6Y of the A5 peptide occur during engagement by the 1D4 TCR. Overlaid wire-frame representations of the A5 peptide in the L^{d}α1α2-A5 complex are shown before (yellow carbons) and after (green carbons) engagement by the 1D4 TCR. Changes in the rotamers of the p4Y and p6Y are indicated with arrows. To demonstrate the quality of the electron density establishing these conformation changes, stereo (cross-eyed) representations of the 2*Fo-Fc* electron densities maps contoured at 1.5 σ around the peptide in the region of p4Y and p6Y are shown before (*B*) and after (*C*) TCR engagement. Use crossed eyes for a three-dimensional merged view of *B* or *C*.

the total 257 atom-to-atom contacts in the TCR footprint (Fig. 4*D* and Dataset S2).

The 1D4 TCR L^d-A5 structure helps to explain the heavy selection of the CDR3β motif in the repertoire of AH1-A5 cross-reactive CD8 T cells (Fig. 1*B*). The motif forms a compact loop at the very tip of the 1D4 CDR3β (Vβ93–96, DGDY) facilitated by the flexibility imparted by the Vβ G94 and stabilized by several H-bonds within the loop (Fig. 6*C*). It settles on the complex using multiple H-bonds and vdW interactions (>50% of the total TCR interactions with the ligand) and contacts each of the surface-exposed amino acids of the peptide: p4Y, p6Y, p7H, and p8Q (Fig. 6*C* and Dataset S2).

Finally, our structures do not tell us directly why the 1D4 T cell and so many of the other AH1/A5 cross-reactive TCRs engage the L^d-AH1 with low affinity, since we have not solved the structure of this complex. One possibility is that AH1 is locked in its position in L^d and therefore the TCR finds a different low-affinity docking mode to account for AH1 weak stimulation. Another, perhaps more likely, possibility is the p4Y and p6Y side chains in L^d-AH1 can only partially complete the required high-affinity conformational changes and therefore can only bind the TCR with low affinity (i.e., the engagement is similar, but weakened). Remodeling

of the AH1 peptide bound to L^d provides at least some support for this second possibility.

Fig. 6*D* shows the p4Y, p5A, and p6Y portion of the A5 peptide from the 1D4 TCR L^{d}α1α2-A5 structure overlaid with a
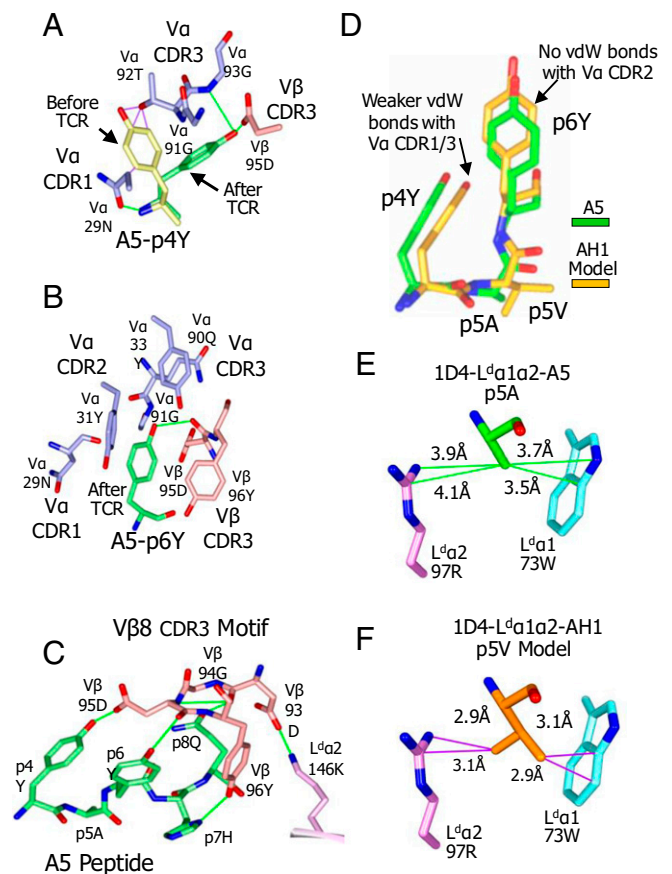
Fig. 6. TCR interactions with the reconfigured A5 peptide and limitations for reconfiguring the AH1 peptide. (*A*) The large rotational movement of the p4Y side chain is required for productive TCR interaction. The p4Y of A5 peptide is shown before (yellow carbons) and after (green carbons) TCR contact as in Fig. 5. The new position of the p4Y side chain avoids clashes with 1D4 Vα (violet carbons) while establishing multiple new productive contacts with Vα and Vβ (pink carbons) that include 2 H-bonds (green lines), as well as vdW interactions. (*B*) Repositioning of the A5 p6Y aligns its side chain for interaction with the 1D4 Vα and Vβ. The side chain of the repositioned p6Y (green carbons) in the L^d-A5-1D4 complex is shown, making many productive contacts with Vα CDR1 and CDR3 (violet carbons) and with Vβ CDR3 (pink carbons). (*C*) The common motif in the 1D4 TCR Vβ8.3 CDR3 is critical for interaction with L^d-A5. Shown are the four Vβ8.3 CDR3β amino acids, Vβ 93–96 (pink carbons), composing the motif shared with many AH1/A5 cross-reactive T cells making extensive contact with the A5 peptide from p4 to p8 (green carbons), which includes many vdW interactions and H-bonds to each of the four surface-exposed A5 amino acids (green lines), as well as a salt bridge (green line) to L^{d}α2 146K (magenta carbons). (*D*) Similar rotations of the p4Y and p6Y side chains of the AH1 peptide to those found in the A5 peptide bound to the 1D4 TCR produce different structures. Shown is a wire-frame representation of the (TCR bound) p4 to p6 A5 peptide (green carbons) over laid with a model of same amino acids from the L^d-AH1 complex (yellow carbons) in which p4Y and p6Y have been given the same rotamers as in the A5 peptide. (*E*) Interaction of p5A of the A5 peptide with the L^d p5 pocket. Wire-frame representations of L^{d}α1 73W (cyan carbons) and L^{d}α2 97R (magenta carbons) interactions with p5A on the 1D4 TCR complex. The four closest atom-to-atom vdW interactions are shown (green lines) with their lengths. (*F*) A p5V would clash with the p5 pocket. Same as *E*, but a model of the p5V (carbons orange) has replaced p5A in the A5 peptide. The four closest interactions are shown as purple lines to indicate the lengths are too short for vdW bonds.

p4Y, p5V, and p6Y from the L^d-AH1 structure in which the p4Y and p6Y side chains have been remodeled to have the same rotamers as the TCR-engaged A5 peptide, while leaving the AH1 peptide backbone unchanged. The rotations do not bring the AH1 tyrosines into the same positions relative to the TCR as those in A5. The shifted position of p4Y has weakened many of its 34 vdW bonds with the TCR Vα CDR1 and CDR3 listed in Dataset S2. The shifted p6Y has lost all contact with Vα CDR2. Fig. 6 *E* and *F* show how the repositioning of the AH1 backbone to bring the rotated p4Yand p6Y into the high-affinity position is disfavored. Fig. 6*E* shows that the structure of L^{d}α1α2-A5 bound to the 1D4 TCR the side chain of p5A makes ideal vdW interactions with L^d 73W and 97R in the L^d p5 pocket. Modeling a V at p5 on the A5 backbone pushes its side chain deeper into the p5 pocket (Fig. 6*F*) and leads to interactions with 73W and 97R at distances as short as 2.9 to 3.1 Å (Fig. 6*F*, purple lines), violating the minimal distances set by the vdW radii of the C and N atoms involved (3.4 Å for C-to-C and 3.25 Å for C-to-N interactions). We conclude from these analyses that the AH1 peptide would be unable to assume the high-affinity position of the A5 peptide. However, by making similar rotational changes in p4Y and p6Y, the interference with TCR binding could be relieved and a possibly low-affinity confirmation might be achieved.

Discussion

The use of self-TAAs with substitutions to improve the antitumor responses of CD8 T cells has a long history and various strategies have been used to produce these modified epitopes that are stronger stimulators of the T cells than the natural epitopes (5, 40–43). The success of these modified self-TAAs as tumor vaccines has been unpredictable and they have met with mixed results (16, 44–46). One of the challenges in creating effective modified self-TAAs has been finding substitutions that that remain highly cross-reactive with the repertoire of T cells that recognize the unmodified native self-TAA, so that vaccination will raise a CD8 T cell repertoire that can attack the tumor via the natural epitope.

Our previous studies (21–24, 26–28, 47) and those presented here show how the BALB/c CT26 colon carcinoma has been a good model for developing strategies to convert weakly immunogenic self-TAAs into immunogenic ones that remain highly cross-reactive with the native TAA. The AH1 self-TAA peptide is presented by the MHCI molecule L^d. As with many self-TAAs (48), it is poorly expressed in most somatic tissues, but is strongly expressed in the CT26 tumor and many other BALB/c tumors (20, 21). Immunization with the AH1 peptide, even using strong adjuvants, raises a CD8 T cell repertoire with limited expansion and poor differentiation into cytotoxic effectors, resulting in no protection from subsequent tumor challenge. A similar ineffective AH1-specific repertoire was found in CT26 TILs during unabated growth of tumors of unimmunized mice.

Screening peptide libraries with an L^d-AH1–specific T cell clone, known as "CT" and isolated from mice vaccinated with irradiated CT26 cells expressing GM-CSF, identified a set of peptides that were much more stimulatory for this T cell clone than AH1 (24). However, the efficacy of the peptides varied greatly in vaccination trials. The most effective peptide (A5), harboring a single substitution of valine (V) to alanine (A) in the p5 position, did not change the L^d binding affinity to the peptide, suggesting that its effectiveness was related to improving TCR recognition in the T cell repertoire rather than L^d binding. Immunizations with A5 and other library peptides all produced expanded, differentiated CD8 T cell responses detected with L^d tetramers containing the immunizing modified AH1 peptide; but only in immunizations with the protective peptides, like A5, were these T cells highly cross-reactive with L^d-AH1 tetramers. High-throughput TCR Vβ sequencing of cross-reactive T cells raised by A5 immunization showed that they were very similar to those raised either by immunization with AH1 and those from the CT26 TIL of unimmunized mice. Thus, the effectiveness of A5 as a vaccine was not primarily due to the expansion of a new set of cross-reactive T cells or of a minor set of AH1 cross-reactive T cells, but rather due to its ability to drive the same T cells that responded to AH1 to expand further and to differentiate into CTL effectors. We conclude that the low-affinity L^d-AH1–specific T cells could be effective CTLs for the AH1-expressing tumor cells provided they were previously expanded and differentiated with a high-affinity cross-reactive peptide.

In the present report we have presented biophysical and structural studies establishing why this single substitution in the A5 version of the AH1 peptide so improves the L^d-peptide as a ligand for the AH1-specific CD8 T cell repertoire. Our initial hypothesis was that somehow changing A for V at p5 of the peptide enabled it to assume a conformation that was better than AH1 at engaging these T cells. In the studies presented here, we used the TCR from the 1D4 T cell that much better represents the broadly cross-reactive AH1/A5-specific repertoire, than the CT TCR cell used in our original studies. The 1D4 TCR was also low affinity for AH1, as expected for a self-TAA. Our TCR binding studies also established that the 1D4 TCR had a much higher affinity for the L^d-A5 ligand than the L^d-AH1 ligand. Furthermore, SPR studies revealed two-phase binding kinetics consistent with a conformational change during the binding of the TCR changing a low-affinity interaction to a high-affinity one.

Our crystallographic studies suggested the nature of the conformational changes predicted by SPR. They confirm that the p5 amino acid is pointed down into the L^d peptide binding groove and that the two flanking tyrosines (Ys) at p4 and p6, essential for T cell responses, are prominently exposed on the L^d-peptide surface. Comparing the crystallographic structures of L^d bound to each peptide prior to TCR engagement shows how the p5V-to-A mutation altered the position of the A5 peptide backbone within the L^d peptide-binding groove, stabilizing the structure of the side chain of the adjacent tyrosine at p6. The structure of the 1D4 TCR bound to L^d-A5 shows that, upon TCR binding, the side chain of p6Y makes a small additional conformational change, but the p4Y now makes a dramatic rotational change, both required to fully accommodate the TCR. These structures can explain the high affinity of the 1D4 TCR for L^d-A5 ligand, the second-order TCR binding kinetics, and the poor binding of the TCR to L^d-AH1, which apparently has difficulty completing these conformational changes. They also explain the heavily selected CDR3β motif during AH1/A5 immunization, since this motif is the major TCR contact with the peptide, not only with p4Y and p6Y but also with p7H and p8Q, the other two predominantly surface-exposed peptide amino acids. We were unable to solve the structure of the 1D4 TCR bound to the low-affinity L^d-AH1 ligand, but our structures point out why this peptide cannot assume conformational changes equivalent to those seen with the A5 peptide.

While our studies have delved deeply into only one self-TAA, our results suggest a general strategy for avoiding pitfalls on the way to identifying self-TAA with modifications that are more likely to yield peptides with therapeutic potential. First, our successful modification was not in a surface-exposed peptide amino acid within the TCR footprint, but rather in an amino acid in the center of the peptide not exposed on the surface (p5). In fact, substitutions we made in surface amino acids within the TCR footprint usually led to loss of cross-reactivity with the native AH1 peptide (24, 27). Unlike peptides bound to MHCII, which depend on hydrogen bonds between conserved MHCII amino acids and the peptide backbone along its entire length, peptides bound to MHCI often have much more freedom of movement between their ends, influenced by the length of the peptide and the side chains of its central amino acids within the MHCI binding groove. Alteration of amino acids that are buried in the MHCI groove can change the configuration of adjacent

Wei et al.
Structures suggest an approach for converting weak self-peptide tumor antigens into superagonists for CD8 T cells in cancer

PNAS | 7 of 10
https://doi.org/10.1073/pnas.2100588118

surface-exposed amino acids without changing their sequence (49–51).

Second, tyrosines like the two in the AH1 peptide can contribute to TCR binding in multiple ways. Their aromatic rings offer a large area for vdW interactions and their hydroxyl group can form H-bonds. Tyrosines are often found at the interface between TCRs or antibodies and their ligands (35–39), and in our structure, the repositioned tyrosines form the major site of TCR interaction. These results suggest that self-TAAs with surface-exposed tyrosines or other large amino acids with multiple conformations (e.g., tryptophan, phenylalanine, or arginine) might be more susceptible to manipulation by adjacent anchor substitutions. There are several other examples of peptide or TCR aromatic amino acids undergoing large conformational change at the TCR/ligand interface (37, 52). Given the large number of self-TAAs now identified in tumors of various tissues (48), preselecting tissue-specific self-TAAs found in multiple patients containing these exposed large, malleable amino acids within the usual TCR footprint should be possible.

Our studies also point out the value of a prior thorough knowledge of the self-TAA–specific CD8 repertoire in the TILs of patients with similar TAA-expressing tumors and a common MHC allele (e.g., HLA-A2) helping to avoid modifications that improve the epitope for only a single T cell, but not the general self-TAA–specific repertoire (53, 54). This approach is now feasible with the recent development of high-throughput TCR sequencing techniques (53, 55), multiple robust TCR$^-$ T cell tumor cell lines for creating easily maintained TCR-transduced T cell avatars (56, 57), standard procedures for using MHCI-peptide tetramers to enrich the peptide-specific T cells (58), and methods for screening insect cell and yeast-displayed MHCI-peptide libraries with soluble TCRs to find high-affinity substitutions in self-TAAs (34, 47, 59).

Materials and Methods

TCR Staining of Peptide-MHC–Expressing Insect Cells. SF9 insect cells were plated at 2×10^6 cells per well in six-well plates and infected with 2 multiplicity of infection of baculovirus expressing L^d-βgal-, L^d-AH1, or L^d-A5. Two days later these insect cells were stained with antibodies recognizing mouse L^d (28.14.8s), gp64 (AcVI; eBiosciences), and soluble fluorescent TCR molecules (1D4 TCR). TCR molecules were expressed in the modified pBacp10pH vector (60) and supernatants were passed over an affinity column conjugated to a TCR-β–specific antibody (H57-597) and a Superdex-200 sizing column. TCR proteins were multimerized using a biotinylated Cα-specific antibody (ADO-304) and streptavidin-AF647 (Invitrogen), as described previously (47). Cells were analyzed on a CyAn flow cytometer (Beckman Coulter) or FACSCalibur (BD Biosciences) and data were processed using FlowJo software (Tree Star).

L^d Tetramer Staining. R-PE–conjugated L^d-tetramers were produced in-house, as described previously (23). Dual tetramer staining was carried out using covalently linked peptide L^d tetramers, as described previously (26). Splenocytes were incubated at room temperature for 90 min with a peptide-loaded tetramer, FcR antibody (2.4G2), viability-discriminating agent 7-aminoactinomycin D (7-AAD; Sigma), and fluorochrome-conjugated Abs (BioLegend) against CD8 (53–6.7), CD11a (M17/4), CD4 (RM4-5), B220 (RA3-6B2), and IA/IE (M5/114.15.2). Cells were analyzed on a CyAn flow cytometer (Beckman Coulter) or FACSCalibur (BD Biosciences) and data were processed using FlowJo software (Tree Star).

Intracellular Cytokine Staining. One week following the second vaccination, splenocytes (2×10^6) were stimulated with the indicated peptide and GolgiStop in 96-well plates for 5 h according to the manufacturer's instructions (BD Cytofix/Cytoperm Plus Fixation/Permeabilization Kit; BD Pharmingen). Cells were stained with surface Abs against CD28, B220, CD4, IA/IE, and CD11a. Following cell fixation and permeabilization, cells were stained with antibody against mouse IFN-γ for 1 h at 4 °C. The frequency and number of IFN-γ$^+$ T cells was determined and corrected for background staining with βgal-vaccinated mice stimulated with the same peptide.

TCR Sequencing and Analysis. Mice were immunized and T cells were isolated from splenocytes. Approximately 1×10^5 CD8$^+$ AH1-tet$^+$ T cells were sorted,

mRNA was isolated using an RNAeasy Mini Kit (Qiagen), and first-strand cDNA was generated using random hexamers and SuperScript III reverse transcriptase (Invitrogen). High-throughput sequencing of PCR products was carried out as described for all Vβ8 family members. Amplicons of 300 to 400 bp were quantified by fluorescent measurement using the QubiT dsDNA HS assay (Invitrogen). Equimolar pools of barcoded amplicons were templates in an emulsion PCR using the 454 GS FLX titanium system (Roche Applied Science) according to the manufacturer's recommendations. Sequences were divided into databases according to the source of AH1-specific T cells.

Tumor Challenge. Six- to 8-wk-old female BALB/cAnNCr mice were purchased from the National Cancer Institute/Charles River Laboratories. All animal protocols were reviewed and approved by the Institutional Animal Care and Use Committee at National Jewish Health. Mice were vaccinated twice, 1 wk apart, as described previously (22). One week following the second vaccination, mice were challenged with 5×10^4 CT26 tumor cells subcutaneously in the hind flank. Tumor-free survival was assessed by palpation of the injection site, and mice were killed when the tumors reached 100 mm^2.

Statistical Analyses. Tumor-free survival was analyzed on Kaplan–Meier survival plots and statistical significance was analyzed with Prism v4.0, GraphPad Software, using the log-rank test. Other analyses were conducted using an unpaired two-tailed Student t test. $P \leq 0.05$ were considered statistically significant and error bars represent the SEM unless otherwise noted. The crystallography statistics are standard and included in *SI Appendix*, Table S1.

Surface Plasmon Resonance. The binding analysis was performed using a BIAcore 2000 equipped with an SA sensor chip as previously reported (61). Briefly, ~2,000 RUs of biotinylated L^d-AH1 and L^d-A5 complexes were immobilized to different flowcells linked with streptavidin. Various concentrations of soluble 1D4 TCR were injected sequentially through the flowcells for 60 s and the SPR signal was recorded. To confirm the biphasic kinetics of 1D4 TCR recognition of L^d-A5, ~2,000 RUs of biotinylated 1D4 TCR were immobilized to the chip. Various concentrations of soluble L^d-A5 were injected sequentially through the flowcells for 60 s and the SPR signal was recorded. The kinetic analyses were done with the standard BIAEval software (v4.1) that comes with the instrument.

Protein Expression and Purification. Recombinant 1D4 TCR was produced as described previously (37, 62). Briefly, the α-chain and β-chain of 1D4 TCR were expressed in *Escherichia coli* BL21 (DE3) cells as inclusion bodies, which were subsequently isolated, washed in Triton X-100, and dissolved in 20 mM Tris pH 8.0, 0.5 mM EDTA, 1 mM DTT, 8 M Urea. Equal amounts of α- and β-inclusion bodies were then refolded by rapid dilution in 100 mM Tris pH 8.0, 5 M Urea, 2 mM EDTA, 400 mM L-Arginine–HCl, 5 mM reduced glutathione, 0.5 mM oxidized glutathione for 48 h at 4 °C. The refolded mixture was dialyzed for 12 h against 20 volumes of 10 mM Tris pH 8.0 and 0.1 M Urea, then against 20 volumes of 10 mM Tris pH 8.0 for 12 h at 4 °C. The 1D4 TCR complexes were purified by anion-exchange chromatography on a MonoQ column (GE Healthcare) eluting with a salt gradient to 1 M NaCl in 10 mM Tris pH 8.0.

The full-length L^d and β2m were purified and refolded from *E. coli* BL21 (DE3) inclusion bodies as described previously (63). Briefly, aliquots of inclusion bodies containing L^d and β2m were dissolved separately in a solution of 20 mM Tris pH 8.0, 0.5 mM EDTA, 1 mM DTT, 8 M Urea. L^d, β2m, and peptide were then mixed in a 1:1:3 molar ratio and the solution was diluted to a final concentration of 100 mM Tris pH 8.0, 2 mM EDTA, 400 mM L-Arginine-HCl, 5 mM reduced glutathione, 0.5 mM oxidized glutathione, and 0.25 mg/mL of total protein for 48 h at 4 °C. The refolded mixture was dialyzed for 12 h against 20 volumes of 10 mM Tris pH 8.0 at 4 °C. The L^d and peptide complexes were purified by anion-exchange chromatography on a MonoQ column (GE Healthcare) eluting with a salt gradient to 1 M NaCl in 10 mM Tris pH 8.0.

Recombinant L^{d}α1α2 with a tryptophan to arginine mutation at position 97 was produced as described previously (33, 34). Briefly, L^{d}α1α2 was expressed in *E. coli* BL21 (DE3) cells as inclusion bodies, which were subsequently isolated, washed in Triton X-100, and dissolved in 20 mM Tris pH 8.0, 0.5 mM EDTA, 1 mM DTT, 8 M Urea. 120 mg Ldα1α2 was refolded together with peptide (5 mg) by rapid dilution in 200 mL 100 mM Tris pH 8.0, 2 mM EDTA, 400 mM L-Arginine-HCl, 5 mM reduced glutathione, 0.5 mM oxidized glutathione for 48 h at 4 °C. The refolded mixture was dialyzed for 12 h against 20 volume of 10 mM Tris pH 8.0 at 4 °C. The Ldα1α2 complexes were purified by anion-exchange chromatography on a MonoQ column

(GE Healthcare) eluting with a salt gradient to 1 M NaCl in 10 mM Tris pH 8.0.

Crystallization. All crystallization trials were performed using the sitting-drop vapor-diffusion method at 4 °C. An equimolar mixture of 1D4 TCR and Ldα1α2 were concentrated to 10 mg/mL before the crystallization trials. 1D4 TCR-Ldα1α2-A5 complex was crystallized in 1.0 M lithium sulfate, 0.1 M imidazole malate pH 6.5, and 2% (wt/vol) PEG 8000 and was cryogenically frozen in liquid nitrogen in crystallization buffer with 20% (vol/vol) glycerol. Ldα1α2-A5 was crystallized in 1.1 M ammonium tartrate dibasic pH 7.0 and was cryogenically frozen in liquid nitrogen in crystallization buffer with 20% (vol/vol) glycerol. Both full-length L^d-AH1 and -A5 were crystallized in 0.2 M sodium malonate pH 5.0, 15 to 20% PEG 3350 (wt/vol), and 5% 1, 6-Hexanediol was cryogenically frozen in liquid nitrogen in crystallization buffer with 20% (vol/vol) glycerol.

X-Ray Data Collection, Processing, and Refinement. The diffraction datasets were collected at the Shanghai Synchrotron Radiation Facility (Shanghai, China) on beam line BL17U1/BL18U1/BL19U1 and at the Advanced Light Source (Berkeley, CA) on beam line 8.2.2. The diffraction data were processed using the HKL2000/3000, iMosflm program 6 (64) and Aimless Pointless in the CCP4 software suite 7 (65). All structures were determined by molecular replacement using the program Phaser (66); For 1D4 TCR-Ldα1α2-A5 complex structure determination, the 42F3 TCR and Ldα1α2 structure (PDB ID code 3TJH) were used as a search model. For full-length L^d-AH1 and -A5 structure determination, the full-length L^d structure (PDB ID code 1LDP) was used as a search model. The models from the molecular replacement were built using Crystallographic Object-Oriented Toolkit, program 9 (67) and subsequently subjected to refinement using Phenix software (68). Crystallography diffraction data collection and refinement statistics are summarized

in *SI Appendix*, Table S1. Structure factor and coordinate files were deposited with the RSCB Protein Data Bank with the PDB ID codes listed in *SI Appendix*, Table S1.

Analyses and Graphic Representations of Structures. Protein–protein interactions were analyzed with the NCONT program within the CCP4 Suite (65). Modeling and structural overlays were done using Swiss PDB Viewer v4.1 (69). All graphical representations of structures were made with Discovery Studio Version 3.0, Accelrys Software, Inc. For wire-frame representations, oxygens are red, nitrogens are blue, and carbons are various colors as indicated in the figures or figure legends. Surfaces, ribbons, and tubes are labeled in the figures.

Data Availability. X-ray crystallography data for the four structures reported here have been deposited in RCSB Protein Data bank and are accessible at https://www.rcsb.org/, via PDB ID codes 6L9K (71), 6L9L (72), 6L9M (73), and 6L9N (74). All other study data are included in the article and supporting information.

1. C. H. June, M. Sadelain, Chimeric antigen receptor therapy. *N. Engl. J. Med.* **379**, 64–73 (2018).
2. A. Ribas, J. D. Wolchok, Cancer immunotherapy using checkpoint blockade. *Science* **359**, 1350–1355 (2018).
3. U. Sahin, Ö. Türeci, Personalized vaccines for cancer immunotherapy. *Science* **359**, 1355–1360 (2018).
4. M. Yarchoan, B. A. Johnson 3rd, E. R. Lutz, D. A. Laheru, E. M. Jaffee, Targeting neoantigens to augment antitumour immunity. *Nat. Rev. Cancer* **17**, 209–222 (2017).
5. H. Ebrahimi-Nik *et al.*, Mass spectrometry driven exploration reveals nuances of neoepitope-driven tumor rejection. *JCI Insight* **5**, e129152 (2019).
6. A. Kahles *et al.*; Cancer Genome Atlas Research Network, Comprehensive analysis of alternative splicing across tumors from 8,705 patients. *Cancer Cell* **34**, 211–224.e6 (2018).
7. T. Dao, D. A. Scheinberg, Peptide vaccines for myeloid leukaemias. *Best Pract. Res. Clin. Haematol.* **21**, 391–404 (2008).
8. F. Mohammed *et al.*, Phosphorylation-dependent interaction between antigenic peptides and MHC class I: A molecular basis for the presentation of transformed self. *Nat. Immunol.* **9**, 1236–1243 (2008).
9. M. Mishto, J. Liepe, Post-translational peptide splicing and T cell responses. *Trends Immunol.* **38**, 904–915 (2017).
10. Y. Guo, K. Lei, L. Tang, Neoantigen vaccine delivery for personalized anticancer immunotherapy. *Front. Immunol.* **9**, 1499 (2018).
11. E. Tran *et al.*, Immunogenicity of somatic mutations in human gastrointestinal cancers. *Science* **350**, 1387–1390 (2015).
12. E. Tran *et al.*, T-cell transfer therapy targeting mutant KRAS in cancer. *N. Engl. J. Med.* **375**, 2255–2262 (2016).
13. T. N. Schumacher, R. D. Schreiber, Neoantigens in cancer immunotherapy. *Science* **348**, 69–74 (2015).
14. C. C. Liu, H. Yang, R. Zhang, J. J. Zhao, D. J. Hao, Tumour-associated antigens and their anti-cancer applications. *Eur. J. Cancer Care (Engl.)* **26** (2017).
15. T. Kumai, A. Fan, Y. Harabuchi, E. Celis, Cancer immunotherapy: Moving forward with peptide T cell vaccines. *Curr. Opin. Immunol.* **47**, 57–63 (2017).
16. I. Melero *et al.*, Therapeutic vaccines for cancer: An overview of clinical trials. *Nat. Rev. Clin. Oncol.* **11**, 509–524 (2014).
17. M. R. Parkhurst *et al.*, Improved induction of melanoma-reactive CTL with peptides from the melanoma antigen gp100 modified at HLA-A*0201-binding residues. *J. Immunol.* **157**, 2539–2548 (1996).
18. O. Y. Borbulevych, T. K. Baxter, Z. Yu, N. P. Restifo, B. M. Baker, Increased immunogenicity of an anchor-modified tumor-associated antigen is due to the enhanced stability of the peptide/MHC complex: Implications for vaccine design. *J. Immunol.* **174**, 4812–4820 (2005).
19. D. J. Schwartzentruber *et al.*, gp100 peptide vaccine and interleukin-2 in patients with advanced melanoma. *N. Engl. J. Med.* **364**, 2119–2127 (2011).
20. A. Y. Huang *et al.*, The immunodominant major histocompatibility complex class I-restricted antigen of a murine colon tumor derives from an endogenous retroviral gene product. *Proc. Natl. Acad. Sci. U.S.A.* **93**, 9730–9735 (1996).
21. J. A. McWilliams *et al.*, Age-dependent tolerance to an endogenous tumor-associated antigen. *Vaccine* **26**, 1863–1873 (2008).
22. K. R. Jordan *et al.*, Baculovirus-infected insect cells expressing peptide-MHC complexes elicit protective antitumor immunity. *J. Immunol.* **180**, 188–197 (2008).
23. R. H. McMahan *et al.*, Relating TCR-peptide-MHC affinity to immunogenicity for the design of tumor vaccines. *J. Clin. Invest.* **116**, 2543–2551 (2006).
24. J. E. Slansky *et al.*, Enhanced antigen-specific antitumor immunity with altered peptide ligands that stabilize the MHC-peptide-TCR complex. *Immunity* **13**, 529–538 (2000).
25. K. A. Waugh *et al.*, Molecular profile of tumor-specific CD8+ T cell hypofunction in a transplantable murine cancer model. *J. Immunol.* **197**, 1477–1488 (2016).
26. K. R. Jordan, R. H. McMahan, C. B. Kemmler, J. W. Kappler, J. E. Slansky, Peptide vaccines prevent tumor growth by activating T cells that respond to native tumor antigens. *Proc. Natl. Acad. Sci. U.S.A.* **107**, 4652–4657 (2010).
27. J. D. Buhrman *et al.*, Improving antigenic peptide vaccines for cancer immunotherapy using a dominant tumor-specific T cell receptor. *J. Biol. Chem.* **288**, 33213–33225 (2013).
28. K. R. Jordan *et al.*, TCR hypervariable regions expressed by T cells that respond to effective tumor vaccines. *Cancer Immunol. Immunother.* **61**, 1627–1638 (2012).
29. M. Corr *et al.*, Endogenous peptides of a soluble major histocompatibility complex class I molecule, H-2Lds: Sequence motif, quantitative binding, and molecular modeling of the complex. *J. Exp. Med.* **176**, 1681–1692 (1992).
30. P. Pymm *et al.*, MHC-I peptides get out of the groove and enable a novel mechanism of HIV-1 escape. *Nat. Struct. Mol. Biol.* **24**, 387–394 (2017).
31. F. E. Tynan *et al.*, T cell receptor recognition of a 'super-bulged' major histocompatibility complex class I-bound peptide. *Nat. Immunol.* **6**, 1114–1122 (2005).
32. K. F. Chan *et al.*, Divergent T-cell receptor recognition modes of a HLA-I restricted extended tumour-associated peptide. *Nat. Commun.* **9**, 1026 (2018).
33. L. A. Colf *et al.*, How a single T cell receptor recognizes both self and foreign MHC. *Cell* **129**, 135–146 (2007).
34. J. J. Adams *et al.*, T cell receptor signaling is limited by docking geometry to peptide-major histocompatibility complex. *Immunity* **35**, 681–693 (2011).
35. P. Marrack, J. P. Scott-Browne, S. Dai, L. Gapin, J. W. Kappler, Evolutionarily conserved amino acids that control TCR-MHC interaction. *Annu. Rev. Immunol.* **26**, 171–203 (2008).
36. S. Koide, S. S. Sidhu, The importance of being tyrosine: Lessons in molecular recognition from minimalist synthetic binding proteins. *ACS Chem. Biol.* **4**, 325–334 (2009).
37. L. Yin *et al.*, A single T cell receptor bound to major histocompatibility complex class I and class II glycoproteins reveals switchable TCR conformers. *Immunity* **35**, 23–33 (2011).
38. L. Yin, J. Scott-Browne, J. W. Kappler, L. Gapin, P. Marrack, T cells and their eons-old obsession with MHC. *Immunol. Rev.* **250**, 49–60 (2012).
39. B. D. Stadinski *et al.*, Hydrophobic CDR3 residues promote the development of self-reactive T cells. *Nat. Immunol.* **17**, 946–955 (2016).
40. J. L. Chen *et al.*, Structural and kinetic basis for heightened immunogenicity of T cell vaccines. *J. Exp. Med.* **201**, 1243–1255 (2005).
41. M. J. van Stipdonk *et al.*, Design of agonistic altered peptides for the robust induction of CTL directed towards H-2Db in complex with the melanoma-associated epitope gp100. *Cancer Res.* **69**, 7784–7792 (2009).
42. S. Zaremba *et al.*, Identification of an enhancer agonist cytotoxic T lymphocyte peptide from human carcinoembryonic antigen. *Cancer Res.* **57**, 4570–4577 (1997).

Wei et al.
Structures suggest an approach for converting weak self-peptide tumor antigens into superagonists for CD8 T cells in cancer

PNAS | 9 of 10
https://doi.org/10.1073/pnas.2100588118

43. L. Fong *et al*., Altered peptide ligand vaccination with Flt3 ligand expanded dendritic cells for tumor immunotherapy. *Proc. Natl. Acad. Sci. U.S.A.* **98**, 8809–8814 (2001).

44. F. Madura *et al*., Structural basis for ineffective T-cell responses to MHC anchor residue-improved "heteroclitic" peptides. *Eur. J. Immunol.* **45**, 584–591 (2015).

45. V. Bianchi *et al*., A molecular switch abrogates glycoprotein 100 (gp100) T-cell receptor (TCR) targeting of a human melanoma antigen. *J. Biol. Chem.* **291**, 8951–8959 (2016).

46. I. Bolonaki *et al*., Vaccination of patients with advanced non-small-cell lung cancer with an optimized cryptic human telomerase reverse transcriptase peptide. *J. Clin. Oncol.* **25**, 2727–2734 (2007).

47. F. Crawford *et al*., Use of baculovirus MHC/peptide display libraries to characterize T-cell receptor ligands. *Immunol. Rev.* **210**, 156–170 (2006).

48. N. Vigneron, V. Stroobant, B. J. Van den Eynde, P. van der Bruggen, Database of T cell-defined human tumor antigens: The 2013 update. *Cancer Immun.* **13**, 15 (2013).

49. C. Capasso *et al*., A novel in silico framework to improve MHC-I epitopes and break the tolerance to melanoma. *OncoImmunology* **6**, e1319028 (2017).

50. D. K. Cole *et al*., Modification of MHC anchor residues generates heteroclitic peptides that alter TCR binding and T cell recognition. *J. Immunol.* **185**, 2600–2610 (2010).

51. P. Filipazzi *et al*., Limited induction of tumor cross-reactive T cells without a measurable clinical benefit in early melanoma patients vaccinated with human leukocyte antigen class I-modified peptides. *Clin. Cancer Res.* **18**, 6485–6496 (2012).

52. I. Song *et al*., Broad TCR repertoire and diverse structural solutions for recognition of an immunodominant CD8^{+} T cell epitope. *Nat. Struct. Mol. Biol.* **24**, 395–406 (2017).

53. D. J. Munson *et al*., Identification of shared TCR sequences from T cells in human breast cancer using emulsion RT-PCR. *Proc. Natl. Acad. Sci. U.S.A.* **113**, 8272–8277 (2016).

54. A. Reuben *et al*., Comprehensive T cell repertoire characterization of non-small cell lung cancer. *Nat. Commun.* **11**, 603 (2020).

55. J. S. Sims *et al*., Diversity and divergence of the glioma-infiltrating T-cell receptor repertoire. *Proc. Natl. Acad. Sci. U.S.A.* **113**, E3529–E3537 (2016).

56. J. White, A. Pullen, K. Choi, P. Marrack, J. W. Kappler, Antigen recognition properties of mutant V beta 3+ T cell receptors are consistent with an immunoglobulin-like structure for the receptor. *J. Exp. Med.* **177**, 119–125 (1993).

57. F. Letourneur, B. Malissen, Derivation of a T cell hybridoma variant deprived of functional T cell receptor alpha and beta chain transcripts reveals a nonfunctional alpha-mRNA of BW5147 origin. *Eur. J. Immunol.* **19**, 2269–2274 (1989).

58. A. K. Bentzen, S. R. Hadrup, Evolution of MHC-based technologies used for detection of antigen-responsive T cells. *Cancer Immunol. Immunother.* **66**, 657–666 (2017).

59. M. H. Gee *et al*., Antigen identification for orphan T cell receptors expressed on tumor-infiltrating lymphocytes. *Cell* **172**, 549–563.e16 (2018).

60. J. Kappler, J. White, H. Kozono, J. Clements, P. Marrack, Binding of a soluble alpha beta T-cell receptor to superantigen/major histocompatibility complex ligands. *Proc. Natl. Acad. Sci. U.S.A.* **91**, 8462–8466 (1994).

61. E. S. Huseby, F. Crawford, J. White, P. Marrack, J. W. Kappler, Interface-disrupting amino acids establish specificity between T cell receptors and complexes of major histocompatibility complex and peptide. *Nat. Immunol.* **7**, 1191–1199 (2006).

62. S. Dai *et al*., Crossreactive T Cells spotlight the germline rules for alphabeta T cell-receptor interactions with MHC molecules. *Immunity* **28**, 324–334 (2008).

63. D. N. Garboczi *et al*., Structure of the complex between human T-cell receptor, viral peptide and HLA-A2. *Nature* **384**, 134–141 (1996).

64. T. G. Battye, L. Kontogiannis, O. Johnson, H. R. Powell, A. G. Leslie, iMOSFLM: A new graphical interface for diffraction-image processing with MOSFLM. *Acta Crystallogr. D Biol. Crystallogr.* **67**, 271–281 (2011).

65. M. D. Winn *et al*., Overview of the CCP4 suite and current developments. *Acta Crystallogr. D Biol. Crystallogr.* **67**, 235–242 (2011).

66. A. J. McCoy *et al*., Phaser crystallographic software. *J. Appl. Cryst.* **40**, 658–674 (2007).

67. P. Emsley, K. Cowtan, Coot: Model-building tools for molecular graphics. *Acta Crystallogr. D Biol. Crystallogr.* **60**, 2126–2132 (2004).

68. P. D. Adams *et al*., PHENIX: Building new software for automated crystallographic structure determination. *Acta Crystallogr. D Biol. Crystallogr.* **58**, 1948–1954 (2002).

69. N. Guex, M. C. Peitsch, SWISS-MODEL and the Swiss-PdbViewer: An environment for comparative protein modeling. *Electrophoresis* **18**, 2714–2723 (1997).

70. G. E. Crooks, G. Hon, J. M. Chandonia, S. E. Brenner, WebLogo: A sequence logo generator. *Genome Res.* **14**, 1188–1190 (2004).

71. P. C. Wei, L. Yin, H2-L[d]a1a2 complexed with A5 peptide. *RCSB Protein Data Bank*. https://www.rcsb.org/structure/6L9K. Deposited 10 November 2019.

72. P. C. Wei, L. Yin, 1D4 TCR recognition of H2-L[d]a1a2 A5 Peptide Complexes. *RCSB Protein Data Bank*. https://www.rcsb.org/structure/6L9L. Deposited 10 November 2019.

73. P. C. Wei, L. Yin, H2-L[d] complexed with AH1 peptide. *RCSB Protein Data Bank*. https://www.rcsb.org/structure/6L9M. Deposited 10 November 2019.

74. P. C. Wei, L. Yin, H2-L[d] complexed with A5 peptide. *RCSB Protein Data Bank*. https://www.rcsb.org/structure/6L9N. Deposited 10 November 2019.